Neutronic performance of the MEGAPIE spallation target under high power proton beam

F. Michel-Sendis[a], S. Chabod[b], A. Letourneau[a], S. Panebianco[*,a], L. Zanini[c]

[a] *CEA - Saclay, Irfu/Service de Physique Nucléaire, F91191 Gif-sur-Yvette, France*
[b] *LPSC, Université Joseph Fourier Grenoble 1, CNRS/IN2P3, 38000 Grenoble, France*
[c] *Paul Scherrer Institute, CH-5232 Villigen PSI, Switzerland*

Abstract

The MEGAPIE project, aiming at the construction and operation of a megawatt liquid lead-bismuth spallation target, constitutes the first step in demonstrating the feasibility of liquid heavy metal target technologies as spallation neutron sources. In particular, MEGAPIE is meant to assess the coupling of a high power proton beam with a window-concept heavy liquid metal target. The experiment has been set at the Paul Scherrer Institute (PSI) in Switzerland and, after a 4-month long irradiation, has provided unique data for a better understanding of the behavior of such a target under realistic irradiation conditions. A complex neutron detector has been developed to provide an on-line measurement of the neutron fluency inside the target and close to the proton beam. The detector is based on micrometric fission chambers and activation foils. These two complementary detection techniques have provided a characterization of the neutron flux inside the target for different positions along its axis. Measurements and simulation results presented in this paper aim to provide important recommendations for future accelerator driven systems (ADS) and neutron source developments.

Key words: ADS, liquid metal target, spallation, neutron detector, Monte Carlo simulation

*Corresponding author: stefano.panebianco@cea.fr

1. Introduction

Strong neutron sources are being developed for various applications such as radioactive beams (EURISOL project [1]), neutrino factories [2], neutron imaging [3] or as external sources for energy production or actinide transmutation in Accelerator Driven Systems (ADS) [4]. It is now admitted that the spallation on heavy liquid metal target is the technology able to provide the most intense neutron sources, where neutrons are produced via the interaction of a high power proton beam with the liquid metal. Such targets, however, had never been built nor irradiated in a megawatt proton beam. Therefore, the MEGAPIE (Megawatt Pilot Experiment) initiative [5] was launched in 1999 to design, build and safely operate a Lead-Bismuth Eutectic (LBE) spallation target, to be irradiated at the SINQ facility in PSI [6]. The target was designed to handle a proton beam power deposition of about 1 MW and successfully underwent a 4 month irradiation from august to december 2006. The MEGAPIE project is considered as an essential step on the road-map towards the development of an ADS. Indeed, the spallation target, located inside the sub-critical core as an external neutron supply, is one of the most innovative and challenging components of an ADS. Among all the different issues that have been studied in the MEGAPIE project, the most relevant for the development of a high-power liquid metal target is the interplay between the proton beam and the generation of neutrons. Neutron production efficiency is one of the first objectives of such a target since it is directly related to the neutron economy and the safety of a sub-critical reactor. Several dedicated experiments, based on a simple geometry where a metal target is surrounded by neutron detectors, have already been performed to study the neutron generation per incident proton on various materials [7, 8, 9]. These data, coupled with thin target experiments, have already allowed to put strong constraints on spallation models (c.f. [10] and references therein). Most of these models are nowadays reliable and qualified against a significant number of experimental data. Nevertheless, when dealing with realistic target geometries, the accuracy with which such complex systems are modeled needs a proper validation on its own. The study of neutron production efficiency of a spallation target under proton irradiation depends not only on the target's composition, geometry and proton energy, but more generally on the way in which protons are ultimately converted into neutrons. This latter part is studied with Monte Carlo simulations, in which particle transport plays an essential role. Thus, a precise determination of

the neutron production efficiency of a spallation target relies on a correct and detailed modeling of the scattering and absorption of neutrons and protons inside and outside the target. These effects, which lead to a global modification of the neutron density and energy distribution, depend on the materials contained in the different environments surrounding the target and can drive the design and the composition of the blanket as well as the radioprotection part of the system. Since it is unfeasible to measure directly the overall neutron flux and neutron energy distributions in a complex integral experiment like MEGAPIE, the neutronic performances of the target have been assessed by a series of neutron flux measurements performed at different positions and distances from the spallation target. The results of these experiments are detailed in [11, 12]. In this paper, we only report on the measurement and the analysis performed with a dedicated neutron detector placed inside the target. The analysis is based on a highly detailed simulation of the entire system using the Monte Carlo transport code MCNPX 2.5.0 [14]. All the gathered data, along with the simulations, have finally provided precise information on the neutron generation capabilities of the MEGAPIE target.

2. The MEGAPIE experiment

We present here a brief description of the MEGAPIE target. A more detailed description of the system and its operation can be found in [15]. The target concept is a loop of liquid Lead-Bismuth Eutectic (LBE) inside a structure arranged vertically over a length of about 5 m. It has been conceived in 9 sub-components designed to accept a maximum proton current of 1.7 mA (with a proton energy of 575 MeV). The particularity of the target is the presence of a window to separate the LBE from the proton beam line (figure 1). This is due to the configuration of the SINQ facility where the proton beam comes from the bottom of the target. The LBE circulates from the spallation region to the heat exchanger (in the upper position) via the main in-line electromagnetic pump. Finally, a neutron detector is inserted inside the central rod, along the vertical axis.

Figure 2 shows the actual proton beam current received by the target during the entire irradiation phase. Very rapid variations of the beam intensity were frequent but only few beam stops lasted more than 48 hours. The effective proton current, averaged during the 123 days of irradiation, is $\overline{I_p}$=960 μA, for an average proton energy of 575 MeV.

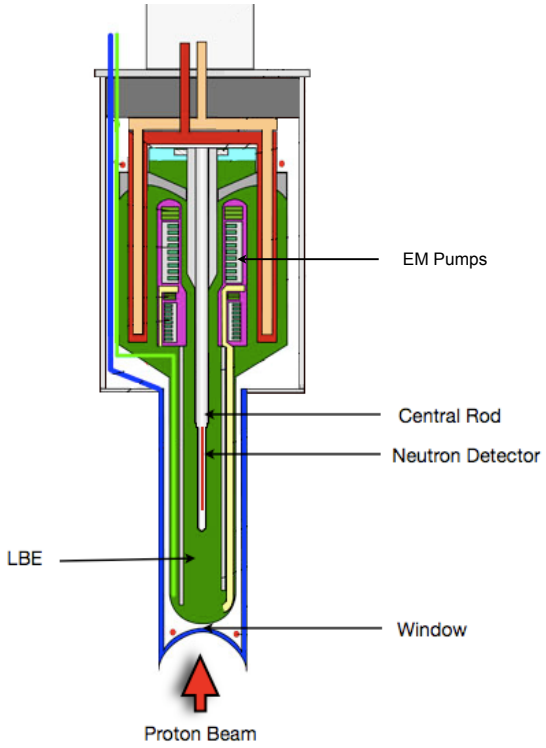

Figure 1: Schematic view of the MEGAPIE target. Proportions are not respected for visibility reasons. The neutron detector is inserted along the vertical axis of the target, inside the *central rod* which is in direct contact with the LBE flow. The upper part of the target houses electro-magnetic pumps that ensure LBE circulation.

2.1. Neutron flux monitoring with fission chambers

An innovative detector has been designed and developed [16] to provide an on-line measurement of the neutron flux inside the target with accuracy better than 5%. This neutron detector is based on micrometric fission chambers (FC) [17] that were developed specifically for MEGAPIE and its very constraining environmental conditions: strong geometrical constraints (the central rod where the detector is placed has a diameter of 20 mm); high temperature (around 690 K with beam-on, decreasing sharply to 500 K with beam off); high level of radiations due to γ-rays (more than $10^{13}\gamma/cm^2/s$) and electromagnetic perturbations due to the electromagnetic pumps. Each FC has a diameter of 4 mm and a total lenght of 8 cm. Fission chambers have been embedded in pairs, side by side, at four different heights (posi-

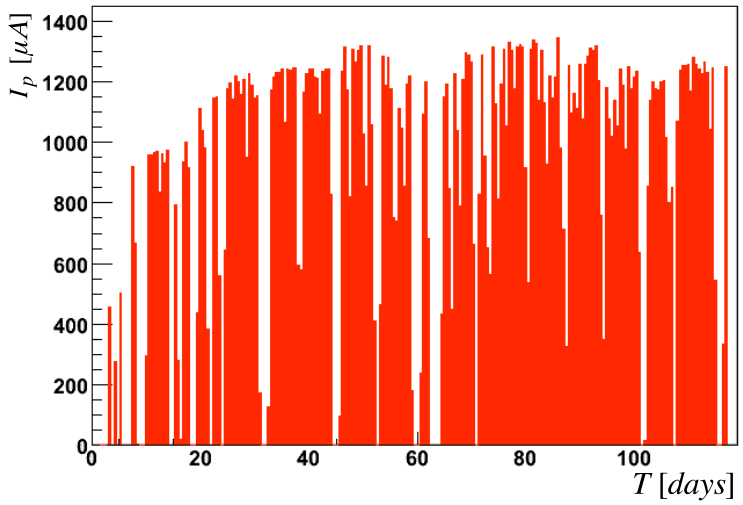

Figure 2: Measured proton beam current during the irradiation phase. The average current received by the target during the 123 days of operation is 960 μA. Data displayed here are 2-day averaged.

tions) along the vertical axis of the central rod over a length of 50 cm (figure 3). For the neutron flux measurement, each position (except the third one) houses an active ^{235}U deposit FC and a FC without deposit (WD) which is used for leakage-current compensation. The first position, at approximately 10 cm from the proton beam Bragg peak, is entirely shielded with pure metallic gadolinium, making that FC only sensitive to epithermal neutrons. For the remaining positions, 99 % of the fission reactions are due to thermal neutrons with energy less than 1 eV. Finally, two FC deposits consisting of ^{241}Am and ^{237}Np have been placed at position 3 to provide information on the incineration of these actinides in a realistic spallation spectrum. In this paper we only concentrate on the analysis of the ^{235}U chambers (positions 1, 2 and 4). Some of the characteristics of FC are summarized in table 1 where we see that each stage is separated by about 13 cm. As shown in figure 3, this configuration gives access to different neutron energy distributions and allows to extract separate information on the neutron production and on the neutron transport parts of the code used to simulate the neutronic behavior of the target.

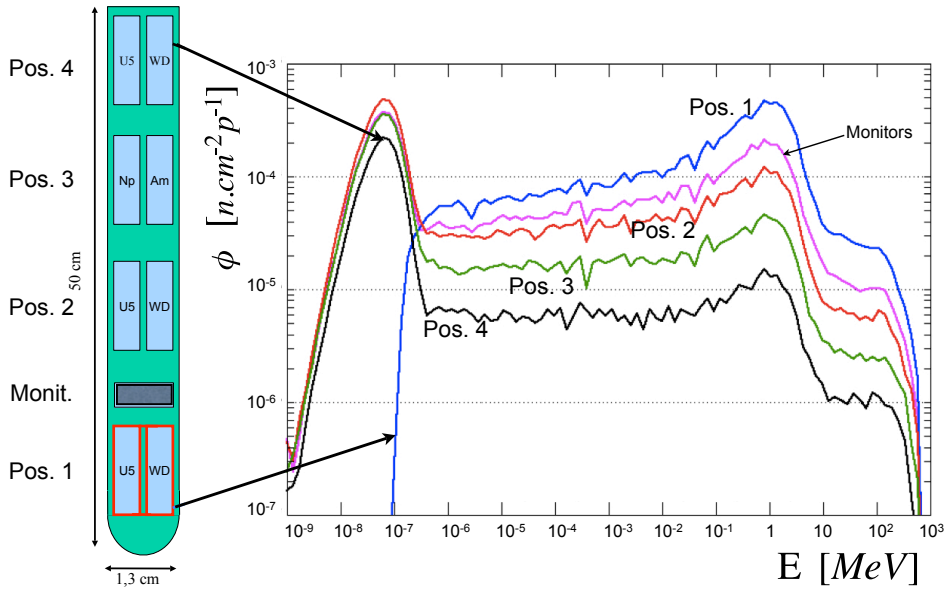

Figure 3: Simplified scheme of the neutron detector placed inside the target. Five vertical positions include 4 fission chamber stages and one monitor box containing activation foils. The two first fission chambers (at the bottom) are shielded with metallic Gd. The simulated neutron spectrum at each of the five positions is shown.

Fission chambers are operated in current mode. The upper plot of figure 4 shows the measured current I as a function of the applied voltage V (calibration curve) for the two FC in position 2 (^{235}U and WD chambers) and a *plateau* regime is clearly visible. The small slope in the plateau of the $I(V)$ curve is due to the electrical resistivity of the FC (including cables). This slope is directly proportional to the temperature of the target and is of the order of few tens nA/V. After correction of the resistive current, in this plateau regime the current measured by a ^{235}U chamber varies very little with the applied voltage and, for a given voltage, is proportional to the number of fissions in the deposit. The leakage current measured by the FC without deposit is of about 10% of the fission current; it is mainly generated by photoelectric effect and activation on the chamber's components.

Table 1: Characteristics of the fission chambers (with deposit) of the MEGAPIE neutron detector. The distances are given from the top of the target window.

Position	1	2	3		4
Distance (cm)	37.1	50.5	60.5		73.6
Fissile isotope	^{235}U	^{235}U	^{241}Am	^{237} Np	^{235}U
Deposit mass (μg)	134.8±0.9	38.9±0.25	198.9±0.7	195.5±7.8	138.7±0.9

For all the fission chambers, the current is recorded by means of a picoammeter, having an accuracy better than 0.1% for the measurement range (from pA to μA). During the irradiation, a calibration curve of all the FC has been performed every 6 hours in order to check that there was no degradation in the response of the detector. This is shown in the lower plot of figure 4, where the ratio of two calibration curves, taken at the beginning and at the end of irradiation, is shown for position 2. One can see that this ratio stays constant within a margin of 2% during the whole irradiation period. This margin can be explained by a small shift in the recorder beam current with respect to the fission current. Finally, all the chambers showed a stable response during the whole irradiation, with the exception of the chamber in the first position (Gd-shielded) where the signal increased dramatically after one week of irradiation, probably due to a loss in the electrical insulation.

The current delivered by the chambers has been recorded every 2 s, together with the proton beam intensity and the temperature inside the central rod. The temperature has been measured at three positions in the neutron detector by means of K-type thermocouples. Figure 5 illustrates the measured currents delivered by the two chambers (with and without deposit) at the second position, together with the proton beam current.

For a given FC position, let I_{U-235} and I_{WD} be the currents measured by the chambers with and without deposit respectively. Since the chambers operate in the *plateau* regime, the fission current I_f is then obtained by the difference : $I_f = I_{U-235} - I_{WD}$. It is proportional to the instantaneous fission rate of the fissile deposit and writes:

$$I_f(t) = \frac{N_f}{\Gamma}\overline{\sigma_f}\phi(t)e^{-\int_0^t \overline{\sigma_a}\phi(t')dt'} \quad (1)$$

where N_f is the initial number of fissile atoms in the deposit, $\overline{\sigma_f}$ is the effective fission cross-section, $\overline{\sigma_a}$ the effective absorption cross-section and $\phi(t)$ is the neutron flux. The exponential term in eq. 1 represents the depletion of the fissile deposit by neutron absorptions. We will refer to this

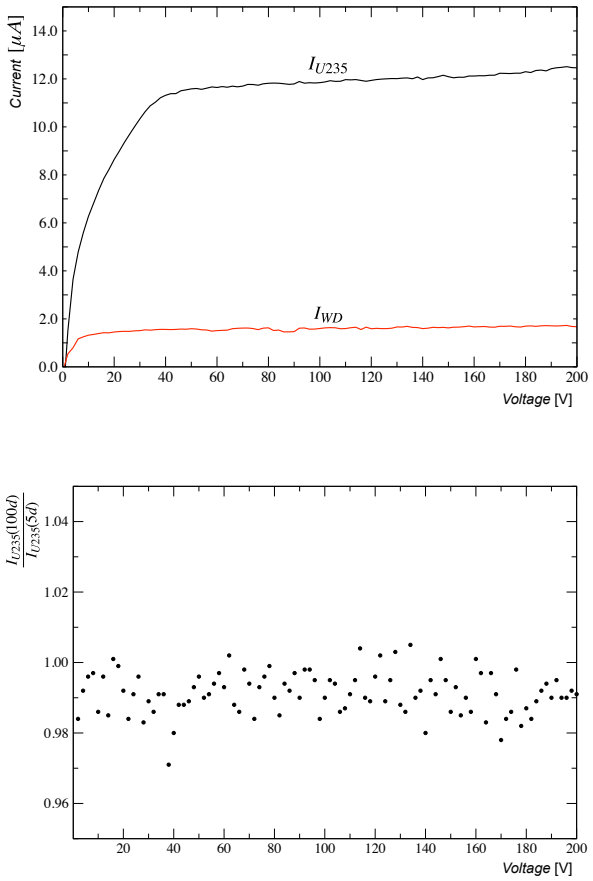

Figure 4: Example of $I(V)$ curves for the chambers in the second position at the beginning of irradiation (top). The ratio of the $I_{U235}(V)$ curves at the beginning (5 days) and at the end of irradiation (100 days) is shown in the bottom figure.

effect as the *burn-up* of the fission chamber. The proportionality coefficient Γ is called the *sensitivity* of the FC. The value of Γ has been measured [18] within 3% precision at the High Flux Reactor of the Institute Laue-Langevin in Grenoble (France) using the same type of chambers, cables and electronics than in MEGAPIE. As shown in [16] the FC sensitivity depends only on the geometry of the chamber and on the gas characteristics (type, pressure, contaminants). Since all chambers are geometrically identical and were built using the same procedure, the value of Γ can be considered common to all

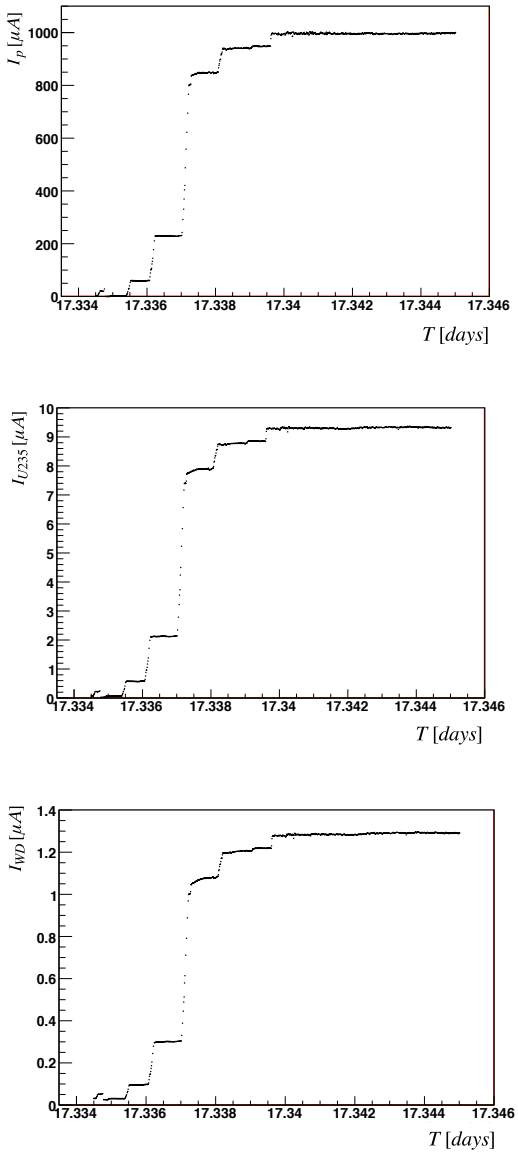

Figure 5: From top to bottom : example of measured proton beam current I_p and chamber currents in the 2nd position; I_{U235} and I_{WD} (with and without deposit).

chambers and is taken to be $(2.85 \pm 0.09) \times 10^{13} s^{-1} A^{-1}$. The error is due both to the 3% uncertainty of ILL measurement, and to the 1% uncertainty in the

gas pressure measurement during the fabrication. The masses of the fissile deposits, and consequently N_f, have been measured by mass spectrometry and validated by gamma spectroscopy [19], resulting in a relative precision better than 1% between all the deposits and an absolute precision of about 1%.

2.2. Neutron fluency measurement with activation foils

In order to set a complete measurement system, we placed inside the neutron detector nine activation foils, consisting of ultra pure metallic discs, 6 mm in diameter. The foils have been arranged inside a titanium box between the first and second FC stage (figure 3). While the fission chambers give an instantaneous information on the neutron flux at different positions along the target, the activation foils, which are gathered around one geographical position, have been chosen for their different sensitivities to neutron energy [20]. The list of neutron-induced reactions and corresponding energy thresholds are given for all the foils in table 2.

Table 2: Characteristics of the activation foils placed inside the neutron detector. *The Al-Co foil is an alloy containing 0.1% in mass of Co. Foil masses were measured at the permil-level precision.

Monitor	Mass (mg)	Reaction	Threshold (MeV) or Range	$T_{1/2}$
Al-Co*	5.576	^{59}Co(n,γ)^{60}Co	Thermal	5.2710 (8) y
Fe	9.889	^{54}Fe(n,p)^{54}Mn	0.7	312.13 (3) d
		^{58}Fe(n,γ)^{59}Fe	Thermal	44.495 (8) d
Ni	11.565	^{58}Ni(n,p)^{58}Co	3-15	70.83 (10) d
		^{60}Ni(n,p)^{60}Co	10	5.2710 (8) y
Rh	8.235	^{103}Rh(n,2n)^{102m}Rh	10	$\sim$ 2.9 y
Mn	20.414	^{55}Mn(n,2n)^{54}Mn	10	312.13 (3) d
Nb	59.083	^{93}Nb(n,γ)^{94}Nb	Therm. + epith.	$2.03.10^4$(16) y
Gd	39.753	^{157}Gd(n,γ)^{158}Gd	Therm. + epith.	stable (EC)
Ti	14.700	^{46}Co(n,p)^{46}Sc	2.5	83.788 (22) d
Y	15.776	^{89}Y(n,2n)^{88}Y	10	106.626 (21) d

Following a thirteen month cooling period after the end of the irradiation, the box containing the monitors has been remotely opened at the PSI Hot Lab and the activation foils have been collected. Four of the nine foils originally present were recovered in integral conditions: Al-Co, Fe, Ni and Rh. The other five were greatly damaged. The mass of the foils has been remeasured and each individual sample went through a gamma spectroscopy analysis using a HPGe detector.

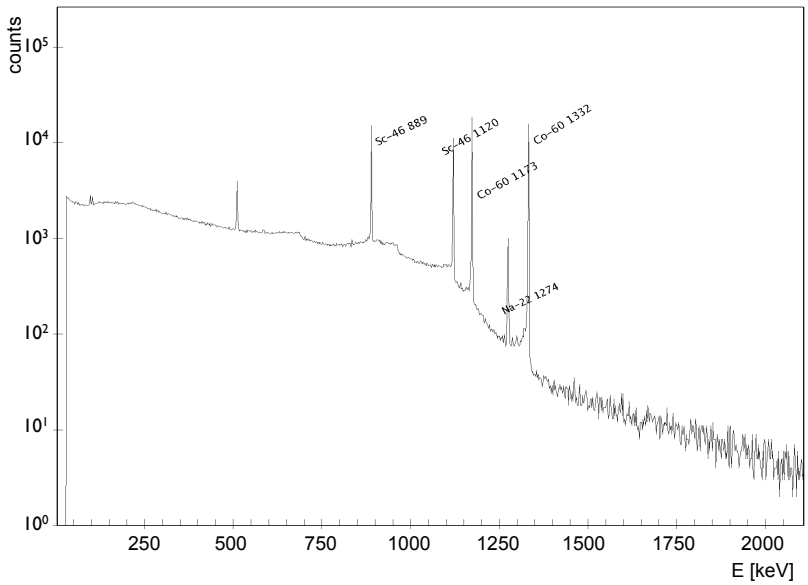

Figure 6: Gamma spectrum of the Al-Co monitor after 20 minutes of data taking. The presence of ^{46}Sc, coming from Ti-monitor fragments cross-contamination, does not perturb the measurement of ^{60}Co activity (known within 2%).

Figure 6 shows, as an example, the measured gamma spectrum of the Al-Co foil. The analysis of the gamma spectrum reveals the presence of ^{46}Sc, coming from a Ti cross-contamination, probably due to the fragmentation of the Ti foil. In the case of the Al-Co foil, however, this does not perturb the measurement of the ^{60}Co activity since all different peaks are well resolved. Similar Mn-54 contamination coming from the Mn foil, also found damaged after the irradiation, has been observed in most of the other gamma spectra. In the case of the Fe foil, this contamination makes unfeasible the study of the ^{54}Fe(n,p)^{54}Mn reaction.

2.3. Modeling of the MEGAPIE target

The analysis of the data needs some input coming from the simulation of the MEGAPIE target. The MCNPX 2.5.0 code has been employed for this simulation and a detailed description of the experiment (geometry, materials, beam) has been developed by the MEGAPIE neutronic team. In the following, we will refer to this simulation as the *reference model*. Fig-

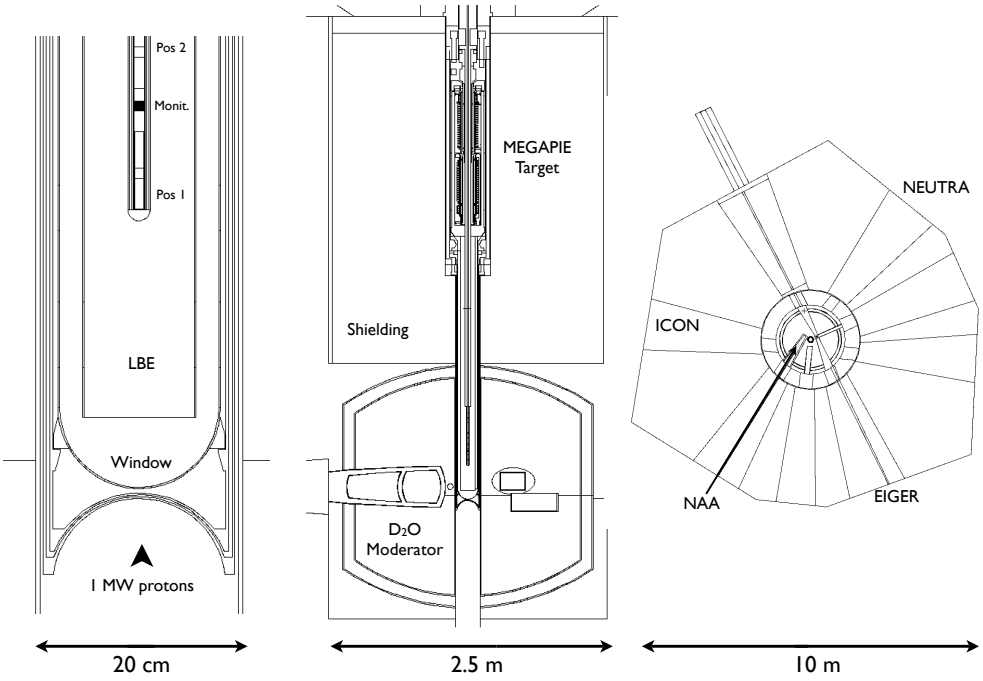

Figure 7: Reference MCNPX model of MEGAPIE. Left : Vertical cut at the central rod position showing the bottom part of the detector and window. Center : vertical cut at the median plane of the target showing the target head, LBE, cold moderator and EM pumps. Right : horizontal cut at the median plane of the SINQ moderator tank showing the different neutron beam lines and irradiation positions which are described.

ure 7 gives a view of a vertical cut of the simulated geometry showing the MEGAPIE target inserted into the moderator tank and a top view of the SINQ geometry around the target. This geometry is a very detailed reproduction of the MEGAPIE target and of the whole SINQ facility, including the D_2O moderator, the cold source, the neutron beam lines, the different irradiation positions offered to the user (NAA, ICON, EIGER, NEUTRA), where even the irradiation capsules have been modeled, as well as all the structures and shielding of the experimental hall. The ancillary systems of the target have been included in the model and all material compositions are described as precisely as possible. It is very important to correctly describe the materials surrounding the spallation zone as they contribute significantly

Table 3: Results of the reference simulation for different quantities relevant for the neutron detector measurements. Effective cross-sections marked with (*) take into account neutron energies up to 60 MeV while the others are integrated only up to 20 MeV, which is the standard energy cutoff in MCNPX data libraries.

Position	$\widetilde{\phi}$ (n/cm^2/s/mA)	Reaction	$\overline{\sigma}$ (b)
1	5.68 10^{13} (0.5%)	^{235}U(n,f)	10.1 (2.3%)
		^{235}U(n,γ)	3.8 (2.0%)
2	3.36 10^{13} (0.7%)	^{235}U(n,f)	204 (2.0%)
		^{235}U(n,γ)	36 (2.0%)
4	8.47 10^{12} (1.0%)	^{235}U(n,f)	299 (2.5%)
		^{235}U(n,γ)	52 (2.5%)
AlCo foil	4.25 10^{13} (0.9%)	^{59}Co(n,γ)^{60}Co	10.9 (5.0%)
Fe foil	4.08 10^{13} (0.9%)	^{58}Fe(n,γ)^{59}Fe	0.28 (5.0%)
Ni foil	4.06 10^{13} (1.0%)	^{58}Ni(n,p)^{58}Co	1.6 10^{-2} (15.0%) *
		^{60}Ni(n,p)^{60}Co	2.9 10^{-3} (28.0%) *
NAA	1.27 10^{13} (0.3%)	^{59}Co(n,γ)^{60}Co	31.5 (5.0%)
		^{58}Ni(n,p)^{58}Co	1.1 10^{-3} (5.0%) *

to the neutron balance. As an example, it has been shown that the boron concentration in LBE (boron is a spallation product) could have a significant impact on the neutron flux measured by the fission chambers [21]. Another effect which has been included in the simulation is the thermal expansion of the target due to its high temperature. The resulting vertical shift has been estimated to be of 1 cm for the target and 1.4 cm for the central rod [22]. A two-dimensional proton beam profile has been derived from the gamma mapping performed on the window of a solid target irradiated in SINQ. This parametrization, which is roughly a double Gaussian shape, takes into account the effects of the interaction with the upstream muon-production target and the collimation system. Finally, in the case of the reference model, the default MCNPX options and the standard data libraries (processed at 300 K) have been used to perform the simulation. We will see in section 4 the impact of changing some default options, including the temperature. The main physical quantities extracted from the reference simulation (neutron flux and effective cross-sections) which are of interest for the analysis of the neutron detector data are given in table 3 where the uncertainty indicated along the simulated value is its statistical error.

In the case of nickel reactions, different cross-section data libraries have been used (ENDF-BVI standard library and special dosimetry files), and so the dispersion observed between these different libraries is taken into account in the overall uncertainty which is given in the table. For the ^{58}Ni(n,p)^{58}Co and ^{60}Ni(n,p)^{60}Co effective cross-sections, since the energy cutoff in the evaluated data is 20 MeV, we have evaluated the correction to be applied and the associated error for the contribution of neutrons above 20 MeV and up to 60 MeV using the TALYS code [23]. This correction is more significant for the ^{60}Ni(n,p)^{60}Co reaction, as shown in figure 8, where the high energy part introduces a relative error on the value of the total cross-section of 28%. In the case of the ^{58}Ni(n,p)^{58}Co the contribution of neutrons above 20 MeV to the reaction rate is mostly negligible.

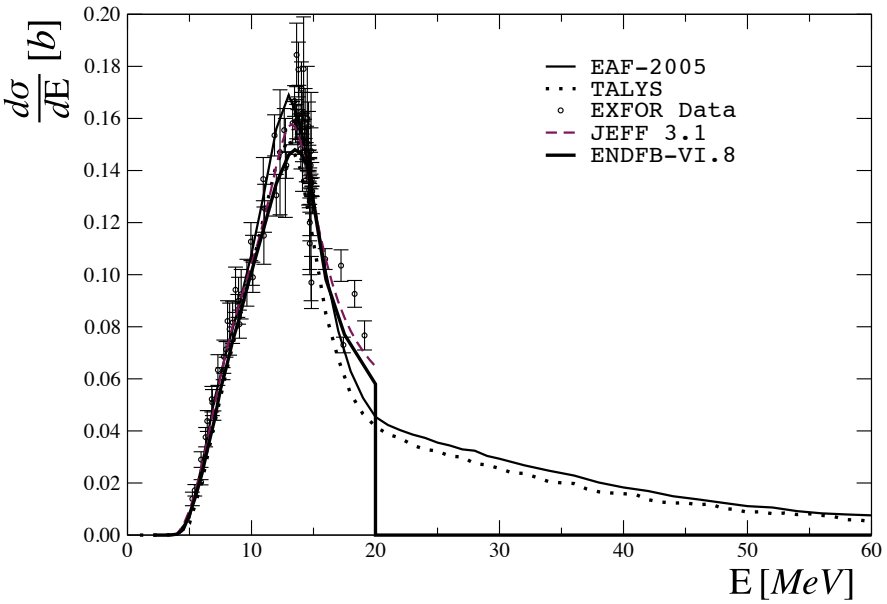

Figure 8: ENDFB-VI ^{60}Ni(n,p)^{60}Co cross-section data used in the reference simulation and the predicted cross-section calculated with the TALYS code. For the sake of comparison, other evaluations are also shown, together with the available experimental data (EXFOR).

Finally, in order to appreciate the sensitivity on a particular energy range of each position in the detectors, we quote in table 4 the distribution of the

neutron population according to 4 ranges in neutron energy E. These ranges are related to the thermal and epithermal regions of the neutron spectrum, to the evaporation phase of the spallation process and to the direct reactions in the nuclear cascade. In the following sections we will discuss how different hypothesis or choices on the simulation parameters may affect the integral and the shape of the neutron spectrum in the different positions and how this is translated into the observables (effective cross-sections and reaction rates) which are used to extract the values of the neutron flux.

Table 4: Neutron population for different energy ranges at the 5 positions inside the neutron detector and the NAA irradiation position. Values are expressed in percent of the total flux at each position.

Position	1 (Gd)	Monit.	2	3	4	NAA
$E > 7$ MeV	4 ±0.1	3 ±0.15	2 ±0.1	1 ±0.1	1 ± 0.1	0.3 ±0.02
500 keV $< E <$ 7 MeV	32 ±0.3	17 ±0.5	12 ±0.2	9 ±0.3	6 ±0.4	0.3 ±0.02
1 eV $< E <$ 500 keV	61 ±0.4	45 ±0.6	38 ±0.4	31 ±0.6	21 ±0.4	3 ±0.04
$E <$ 1 eV	3 ±0.1	35 ±0.5	49 ±0.5	59 ±0.7	71 ±0.8	96.4 ±0.3

3. Data analysis

3.1. Fission chambers analysis

It is expected that the neutron flux ϕ, at any geographical position, is proportional to the proton beam current (this is also an underlying principle of the Monte Carlo simulation itself). We can therefore write $\phi(t) = \widetilde{\phi(t)} \times I_p(t)$, where, for a given position, $\widetilde{\phi}$ is the neutron flux per mA obtained from the simulation.

The neutronic response of the target has been measured by all the fission chambers during the start-up phase of the MEGAPIE experiment, when the LBE composition was still unchanged by the production of spallation residues and the burn-up of the fissile deposits was negligible. In this case, equation 1 can be rewritten as: $I_f(t) = \frac{N_f}{\Gamma}\overline{\sigma_f}\widetilde{\phi}I_p(t)$. Figure 9 shows the expected linear proportionality between I_f and I_p. From these curves one can directly obtain the measured fission rates per mA of proton beam current. These rates are presented in table 5 and compared with the values obtained with the simulation. One can see that the fission rates are systematically over-predicted by at least a factor 2. The calculation to experiment ratio (C/E) depends on the position of the FC and is more pronounced for the

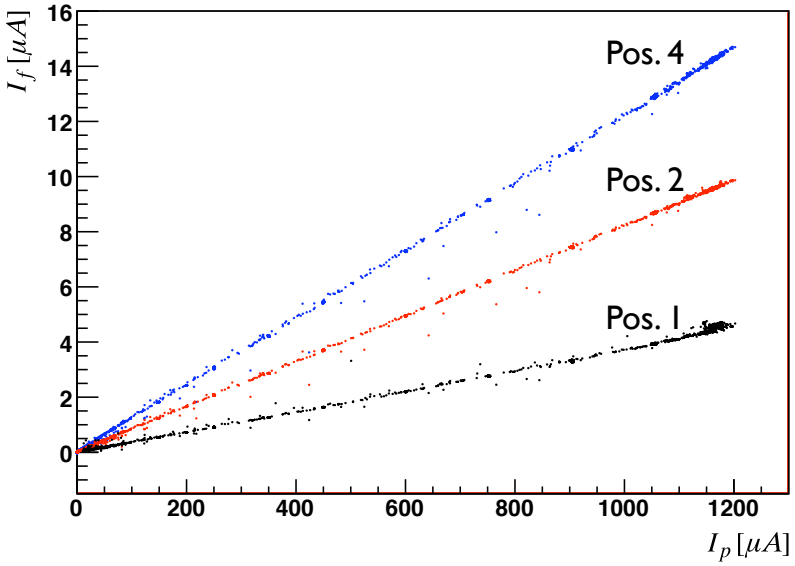

Figure 9: Fission current versus proton current for 1st, the 2nd and the 4th (steeper slope) positions. Data are taken during the first 4 days of irradiation. The linear relation between beam intensity and fission currents is verified.

two uppermost positions, where the proportion of thermal neutrons goes from around 50% (pos. 2) to more than 70% (pos. 4). The C/E ratios given in table 5 could (at this stage of the analysis) be interpreted as an overall neutron production problem to which is added a neutron transport problem which can depend on the position of the FC, and therefore, on the overall description of the geometry of the system. The first problem acts on the integral of the neutron distribution, whereas the second one is related to the neutron distribution itself and, consequently, to the effective cross-sections.

We have first explored the variation of the neutronic response of the chambers along the irradiation period. We do not expect large variations in the response, but the production of neutronic poisons in the LBE could, for example, modify the effective fission rates over time. Let $R(t)$ be the ratio between the measured fission current and the proton beam intensity as a function of time. It is expressed as:

Table 5: Fission rates $\tau_f = \overline{\sigma_f}\widetilde{\phi}$ (in $s^{-1}mA^{-1}at^{-1}$) measured in the first days of irradiation for the different FC positions. The corresponding simulated values are also given. The experimental uncertainty and the statistical error for the simulation is indicated in brackets.

Position	1	2	4
Measured τ_f	$3.04\ 10^{-10}$ (3%)	$2.35\ 10^{-9}$ (3%)	$9.76\ 10^{-10}$ (3%)
Simulated τ_f	$5.80\ 10^{-10}$ (2%)	$6.92\ 10^{-9}$ (2%)	$2.53\ 10^{-9}$ (2.5%)
C/E	1.9 (3.6%)	2.9 (3.6%)	2.6 (3.9%)

$$R(t) = \frac{I_f(t)}{I_p(t)} = \frac{N_f \overline{\sigma_f}}{\Gamma}\widetilde{\phi} e^{-\int \widetilde{\phi} I_p(t') \overline{\sigma_a} dt'} \tag{2}$$

where $\overline{\sigma_a}$ is the effective total absorption cross section, determined by the simulation and which we consider not to evolve with time. The burn-up of the FC uranium deposits at the end of the 4-month irradiation is estimated to be of around 2.8 % and 1.2 % for FC at positions 2 and 4 respectively. Therefore, no large variation is expected on this ratio as a function of time. Figure 10 shows the evolution of this quantity for the 2nd and 4th stages. First, we observe a global decrease of around 5%, which is higher than the expected burn-up for both stages. Since this time-structure is common to all the fission chambers and no degradation of the resistivity of the chamber has been observed, this effect must come from real variations of the target behavior. This is indeed confirmed by thermal-hydraulic analysis where the same time structure (figure 10) is found on the evolution of the heat deposition efficiency in the target over the irradiation [24].

When looking at how the $R(t)$ values are distributed (figure 12), one can see that there are some structures in the distribution that can be related to different periods in time. Although the proton beam intensity is measured upstream the target window, this measurement does not carry any information about the effective number of protons actually hitting the LBE. Depending on the beam configuration and in particular on the beam focusing on the target, the amount of protons interacting in the target, and therefore the number of produced neutrons, can be slightly modified. This point will be discussed in more detail in the next section. At this stage, we assume that the sharp changes in the $R(t)$ distributions are due to changes in the proton beam configuration and we estimate this overall change to be of around 3% between the beginning and the end of the irradiation. On the other hand, we

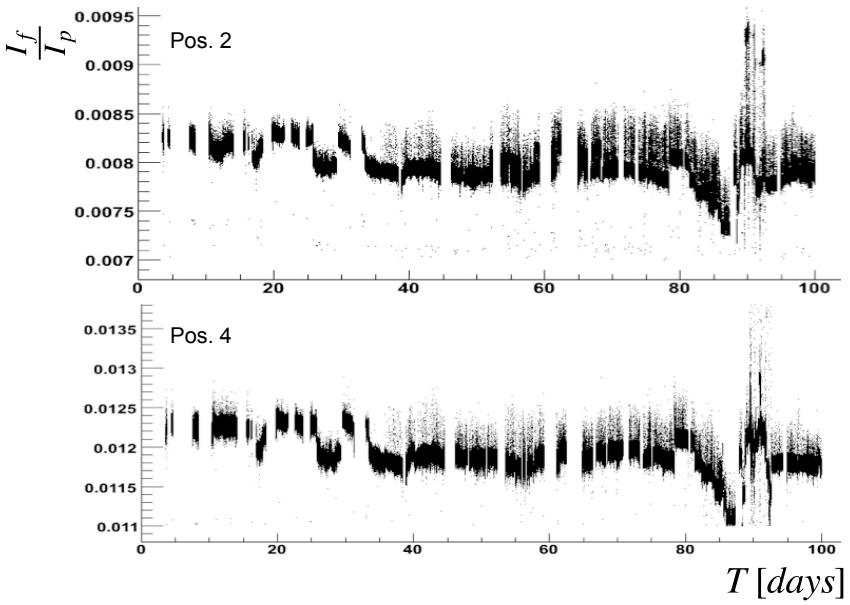

Figure 10: Evolution of $R(t) = I_F(t)/I_p(t)$ (see text), as a function of time for the two FC positions. Errors on the fission currents are not visible on the figure but are contained within the fluctuations. Errors on the beam intensity are not included.

can estimate the uncertainty with which I_p is measured from the full half-width maximum value of the $R(t)$ distribution in a time region where the proton current is stable: this is of the order of 0.3%.

Given these uncertainties, it is difficult to extract deeper information on, for example, the variation of the neutron flux with the ageing of the target and, in particular, the contamination effect in the LBE due to poisons produced in spallation reactions. The most conservative conclusion which can be drawn is that no effect is visible at a level of more than 5% of the value of the neutron flux. Another important point is that, within the same margin of error, we can conclude that the effective neutron reaction cross-sections are constant in time, showing a relatively good stability of the neutron spectra throughout the irradiation.

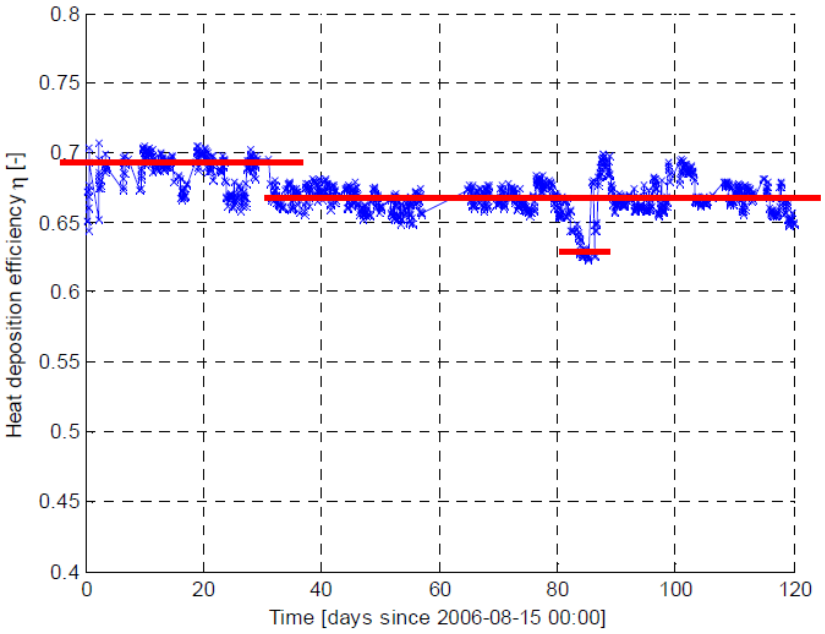

Figure 11: Evolution of the heat deposition efficiency η calculated from the measured thermal-hydralic data over the irradiation time.

3.2. Activation foil analysis

The activation foils provide a different set of measurements and information which complete those obtained with the FC. In particular, they give information on the total neutron fluency received by the neutron detector and can constitute an independent cross-check of the FC calibration. The analysis of the measured foil activities is performed considering that the time evolution of the activity of a gamma emitter (which is created by the reaction $X_1 \rightarrow X_2$) can be expressed by a recursive function which takes into account the proton beam (and therefore the neutron flux) variations. The activity (A_2) of the gamma-emitting nuclide X_2 after a cooling time t is :

$$A_2(t) = \left\{ N_1 \overline{\sigma_1} \sum_i \phi_i (1 - e^{-\lambda_2 (t_i - t_{i-1})}) \right\} e^{-\lambda_2 t} \tag{3}$$

where λ_2 is the decay constant of the gamma-emitter nuclide X_2 and

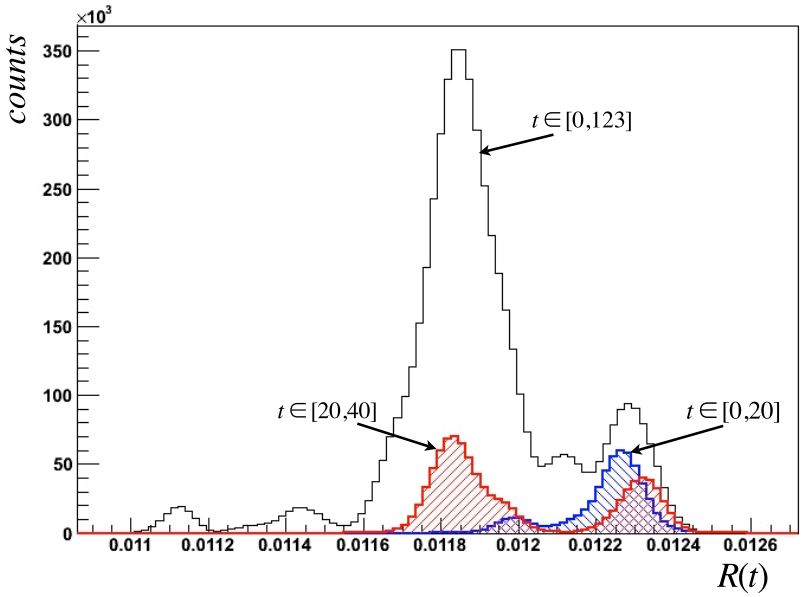

Figure 12: Distribution of the measured values of the quantity $R(t) = I_f(t)/I_p(t)$, shown here for FC position number 4. Different cuts in time (expressed in days) are also indicated inside brackets.

$\overline{\sigma_1}$ the effective cross-section of the reaction $X_1 \rightarrow X_2$. The time $t_i - t_{i-1}$ corresponds to the interval on which we consider that the neutron flux ϕ_i (or the proton beam) can be considered as a constant. In equation 3 the depletion of the parent atoms N_1 is neglected and we consider that $\overline{\sigma_1}$ does not change with time.

Additionally, we have used the CINDER90 code [25], which calculates the evolution of a material under neutron irradiation, to verify that the total gamma activity of each foil at the time of the measurement comes essentially (at least with a 98% contribution) from the activation reaction considered, as is shown in table 6. This ensures that the gamma-activities are not contaminated by other isotopes which are present in the original composition of the activation foils and that equation 3 can be used to deduce the activation rate from the activity measurement.

From the measured activity A_2, we can extract the average activation rate per mA, $\overline{\tau_1}$, given by

$$\overline{\tau_1} = \sigma_1 \overline{\phi} = \frac{A_2}{N_1(1 - e^{-\lambda_2 T_i})e^{-T_c}\overline{I_p}} \tag{4}$$

where we have implicitly written $\widetilde{\phi I_p} = \overline{\phi}$, the average neutron flux for each individual foil, and T_i and T_c are the total irradiation and total cooling time, respectively. In our case it does indeed make sense to extract an average activation rate since the shortest-lived gamma-emitter nuclide we deal with (^{59}Fe) has a much longer half-life (44 days) than the longest beam-down periods in the MEGAPIE irradiation, which were of the order of 1 day. In table 7 we compare these average activation rates ($\overline{\tau}_{\text{meas.}}$) with the ones given by the reference simulation in MCNPX ($\overline{\tau}_{\text{mcnpx}}$).

Table 6: Contribution per reaction to the total gamma activity A_γ of the foils at the time of the activity measurement (calculated with CINDER90).

Reaction	Contribution to total A_γ
^{59}Co(n,γ)^{60}Co	100 %
^{58}Ni(n,p)^{58}Co	99.8%
^{60}Ni(n,p)^{60}Co	98.3%
^{58}Fe(n,γ)^{59}Fe	99.9 %

Table 7: Measured activities, measured average activation reaction rates and corresponding calculated reaction rates for the activation foils. The error given for the measured activities is the total error of the measure, which takes into account the statistical error and the error on the geometrical efficiency of the HPGe detector. In the case of the ^{60}Ni reaction, the simulated value marked with (*) includes neutrons up to 60 MeV.

Monitor	Al-Co	Fe	Ni	
Reaction	^{59}Co(n,γ)^{60}Co	^{58}Fe(n,γ)^{59}Fe	^{58}Ni(n,p)^{58}Co	^{60}Ni(n,p)^{60}Co
Energy range	Thermal	Thermal	3-15 MeV	10-60 MeV
$A_{measured}$ (kBq)	441 (2.1%)	3.1 (8.2%)	377(3.2%)	41 (2.45%)
$\overline{\tau}_{\text{meas.}}$ ($at^{-1}s^{-1}mA^{-1}$)	2.10 10^{-10} (2.1%)	7.0 10^{-12} (8.2%)	3.70 10^{-13} (3.2%)	3.70 10^{-14} (2.45%)
$\overline{\tau}_{\text{mcnpx}}$ ($at^{-1}s^{-1}mA^{-1}$)	4.4 10^{-10} (5%)	1.22 10^{-11} (6%)	7 10^{-13} (15%)	1.2 10^{-13}* (28%)
A_{mcnpx} (kBq)	897 (5%)	5.3 (5%)	720 (15%)	136* (28%)
C/E	2.1 (5.4%)	1.7 (10%)	1.9 (15%)	3.3* (28%)

As already observed with the fission chambers, there is also here an overestimation of the measured activity by about a factor 2 for thermal and fast neutrons. However, one has to note that in the case of activation foils we

would expect the average C/E ratio for thermal reactions (which is around 1.9) to be close to C/E value given by the FC measurement in position 2 (which is 2.9), this FC being the closest to the activation foil position (the anode center of this chamber is only 7 cm distant from the monitor box).

In order to stress again the importance of a very detailed simulation, it has to be noted that in the simulation the activation foils are modeled one by one as they were placed in the experiment. Figure 13 shows the neutron flux at the foil positions. One can clearly see a local drop of almost 40% which is due to the important thermal absorption cross-section of the Gd foil. This shadowing effect, affecting also the closest neighbors (Al-Co, Fe and Ni, in the actual experimental setup), introduces a perturbation in the neutron flux around 10% for the Al-Co foil and 13% for the Fe foil. This correction has to be taken into account when extracting the actual value of the thermal flux from the measured activity of foils which are sensitive to thermal neutrons. For threshold reactions, as the reactions on Ni, which are sensitive only to fast neutrons, the effect can be neglected. Furthermore, if one compares the simulated reaction rates (c.f. table 8) obtained with and without the presence of the Gd foil, an effect up to 40% can be found for reactions sensitive to thermal neutrons.

In the absence of Gd foil we obtain C/E values which vary from 2.4 to 2.9 for the thermal energy range, therefore in better agreement with the C/E obtained for FC. This hypothesis is examined since, in practice, the Gd foil was found fragmented and therefore its position during the irradiation is not known with certainty.

Table 8: Effect of the presence of Gd on the simulated reaction rate of the surrounding foils. The presence of Gd foil has an important effect on thermal reactions which must be taken into account. Rates are given in /s/mA/at. These calculations have been performed with the standard energy curoff 20 MeV and the ENDF-BVI.8 standard library.

Monitor	Reaction	With Gd	Without Gd	Ratio
Al-Co	^{59}Co(n,γ)^{60}Co	4.45 10^{-10} (5%)	6.02 10^{-10} (5%)	1.35 (7%)
Fe	^{58}Fe(n,γ)^{59}Fe	1.22 10^{-11} (5%)	1.75 10^{-11} (5%)	1.43 (7%)
Ni*	^{58}Ni(n,p)^{58}Co	6.71 10^{-13} (5%)	6.73 10^{-13} (5%)	1.00 (7%)
	^{60}Ni(n,p)^{60}Co	8.75 10^{-14} (5%)	9.11 10^{-14} (5%)	1.04 (7%)

4. Discussion

Table 9 summarizes the measured and calculated reaction rates obtained in the previous section, where we have added the results obtained from the

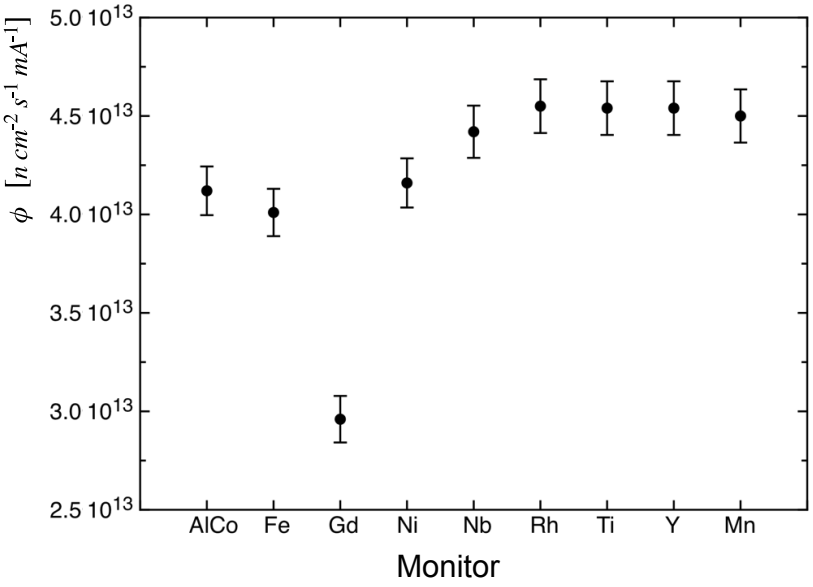

Figure 13: Simulation of the average neutron flux at each foil position inside the box. The error bars, of around 3%, represent the statistical error. In this representation, the upward direction of the vertical axis would be from the right to the left of the figure, the Mn monitor being the closest to the target's window.

Table 9: Comparison between measured ($\overline{\tau_{meas}}$) and simulated ($\overline{\tau_{sim}}$) reaction rates.

Position	$\widetilde{\phi}_{sim}$ (n/cm^2/s/mA)	Reaction	$\overline{\tau_{meas}}$ (/s/mA/at)	$\overline{\tau_{sim}}$ (/s/mA/at)	C/E
1	5.7 10^{+13} (0.5%)	^{235}U(n,f)	3.04 10^{-10} (3%)	5.8 10^{-10} (2%)	1.9 (3.6%)
2	3.4 10^{+13} (0.7%)	^{235}U(n,f)	2.35 10^{-9} (3%)	6.9 10^{-9} (2%)	2.9 (3.6%)
4	8.5 10^{+12} (1.0%)	^{235}U(n,f)	9.8 10^{-10} (3%)	2.53 10^{-9} (3%)	2.6 (3.9%)
Al-Co	4.2 10^{+13} (0.9%)	^{59}Co(n,γ)^{60}Co	2.10 10^{-10} (2%)	4.5 10^{-10} (5%)	2.1 (5.4%)
Fe	4.1 10^{+13} (0.9%)	^{58}Fe(n,γ)^{59}Fe	7.0 10^{-12} (8%)	1.22 10^{-11} (5%)	1.7 (10%)
Ni	4.1 10^{+13} (1.0%)	^{58}Ni(n,p)^{58}Co	3.7 10^{-13} (3%)	7 10^{-13} (15%)	1.9 (15%)
		^{60}Ni(n,p)^{60}Co	3.7 10^{-14} (3%)	1.2 10^{-13} (15%)	3.3 (28%)
NAA	1.27 10^{+13} (0.3%)	^{59}Co(n,γ)^{60}Co	3.19 10^{-10} (3 %)	4.1 10^{-10} (5 %)	1.3 (6%)
		^{58}Ni(n,p)^{58}Co	6.61 10^{-15} (5%)	1.3 10^{-14} (15%)	1.9 (16%)

NAA irradiation station [11]. Figure 14 displays these C/E values as a function of the neutron energy range which is concerned. From this figure we clearly see an overall overestimation of the reaction rates by the reference

simulation for all the neutron energy ranges. The simulation overestimates the experimental data by a factor 2 in the fast and epithermal region and by a factor 2.5 in the thermal region. The same factor 2 also exists for the ^{58}Ni(n,p)^{58}Co reaction in NAA whereas the ^{59}Co(n,γ)^{60}Co reaction only shows a factor 1.3. The latter result agrees with external neutron flux measurements (ICON, NEUTRA and EIGER, fig 7) reported in [12] for which experimental and calculated values agree within 25%. To understand the origin of these discrepancies a large set of tests has been performed in the simulation to check the impact of different parameters and configurations. The results of this study are developed in the following sections where they are classified depending on the neutron energy region on which a significant impact has been observed.

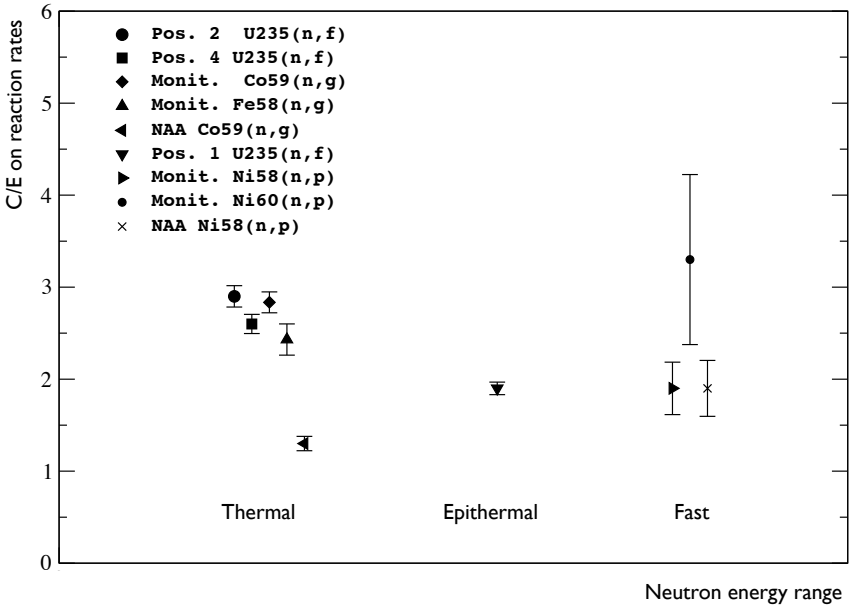

Figure 14: C/E values for the different reaction rates measured inside the target and in NAA.

4.1. Fast neutrons

The fast neutron component of the flux has been measured by (n,p) reactions on ^{58}Ni and ^{60}Ni. The first reaction selects neutrons having energies ranging between 2 MeV and 20 MeV, whereas the second one selects neutrons with energies ranging between 10 and 60 MeV. The neutron fluency measured by the Ni foil is then representative of the amount of neutrons produced during the whole sequence of nuclear reactions induced by the incident proton.

One should consider that due to the small size of the activation foils, the selected solid angle is very tiny. Consequently, the fluency on the foils is very sensitive to the spatial development of the spallation cascade, which depends mainly on how protons hit the LBE and on the angular dependence of the neutron emission. Such an effect can lead to a local reduction of the amount of neutrons without affecting the total number of produced neutrons. To verify whether this effect is present outside the target, we have looked at a Ni activation foil placed in the so-called NAA irradiation station, inside the heavy-water moderator tank [6], and close to the target. The analysis of the ^{58}Ni(n,p)^{58}Co reaction in NAA is reported in [11] and shows a similar C/E value (see table 9) than the one found for the same reaction in the neutron detector. This leads us to conclude that the discrepancy between the simulation and the measurements is not a simple local effect but rather a general trend. First of all, one should keep in mind that thermal-hydraulics measurements have shown that the heat deposited in the target corresponds to the expected beam power[24]. However, most of the proton beam energy is lost by electromagnetic interaction with the LBE, so that thermal-hydraulic measurements are not fully representative of the manner in which protons are converted into neutrons. This raises the general question of the efficiency with which, in the simulation, the incident proton energy is transformed into neutrons. We have therefore explored this point by looking at the influence of the proton beam description on the neutron production and the influence of different models which describe spallation reactions.

4.1.1. Influence of the proton beam description

The MEGAPIE target radius in the proton interaction zone is 10 cm. This distance can be compared to the mean free path of protons inside the LBE, which is around 27 cm. It means that an incoming proton deviating from its incoming trajectory along the beam axis is likely to escape the target without depositing its entire energy in the LBE. The likelihood of such an

event depends on the proton beam angular distribution and its footprint. Firstly, the proton beam is focused in a plane below the target window, in order to avoid the concentration of all the beam power in a single spot. This is especially important for a window-concept liquid target like MEGAPIE, where hot spots on the window have to be avoided to prevent excessive damage of its structure. Because of the beam-line optics, ahead of this focal plane and before entering the target, the proton beam is likely affected by a spread in angular distribution.

Since the angular distribution of the beam has not been measured during the MEGAPIE experiment, this spread is not taken into account in our reference simulation, where all proton trajectories are parallel to the target axis. In the absence of a measured angular distribution, we have simulated a beam spread by defining a cone whose origin is arbitrarily placed 10 cm below the top of the window and with an opening angle θ. Figure 15 illustrates how the angular distribution of the proton beam affects the C/E values of neutron production in different positions along the neutron detector and in NAA. One can observe large variations, up to a factor of three, depending on the opening angle.

It is important to note that effective cross-sections do not vary much with the angle. This means that the main source of this variation in the reaction rate comes from the average neutron flux value, which is itself linked to the spatial development of the cascade inside the LBE. This is confirmed by looking at the total number of neutrons produced per incoming proton as a function of θ (table 10) where one can see that increasing the opening angle causes a decrease of total neutron production. This is due to a raise in the number of protons escaping the target, as can also be seen by the increase of the percentage of neutrons created through (n,xn) reactions on the target structures.

As an example, for a value of θ of 20°, which would give a C/E of 1 for NAA, the loss in total neutron production is 16% while the C/E for the other positions gets closer to 1, still remaining larger than 2. An opening angle of 35° would give a neutron loss around 35% which would have been observed in the MEGAPIE external flux measurements [11, 12], where calculation and experimental values agree within 25%. It must be noted that the absolute value of θ is meaningless in this context since the focal plane has been arbitrarily placed. From this study we can conclude that an angular spread of the beam, although it has not been measured, is a realistic hypothesis that could partially explain the discrepancies observed between simulation

and measurements. A study on the beam divergence in SINQ is currently in progress. From beam transport calculations made on an ideal beam line [**?**], the average divergence from the plane $z = -95$ cm (position of the last collimator) is of a few tenth of mrad. The work to include this effect into the MCNPX model of MEGAPIE is presently ongoing. Very preliminary results indicate an effect on the neutron yeald of a few percent.

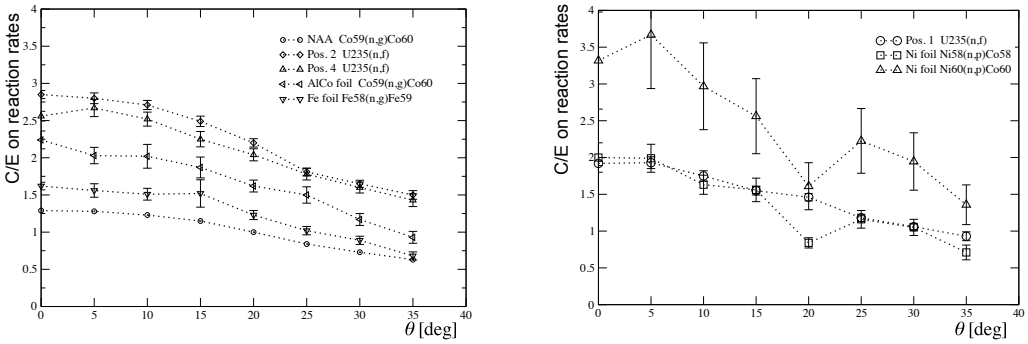

Figure 15: C/E values for reaction rates as a function of the opening angle the proton beam. The left plot concentrates on rections induced by thermal neutrons while the right is related to fast neutrons.

Table 10: From simulation, total number of neutrons produced per incoming proton and percentage of these neutrons created by (n,xn) reactions in the entire MEGAPIE reference geometry, as a function of the proton beam opening angle θ. The statistical uncertainty associated to these values is less than 1%.

Aperture θ (deg)	0	5	10	15	20	25	30	35
Number of neutrons / proton	13.0	12.9	12.6	11.9	10.9	9.9	9.0	8.4
Percentage of (n,xn)	35.7 %	35.5 %	35.2 %	35.6 %	37.1 %	39.2 %	41.1 %	42.7 %

Another beam property that can have an impact on the flux simulation is its footprint on the target. Although a detailed footprint parametrization is used in the simulation, this description comes from a thorough analysis of a previous solid SINQ target[26]. A set of other footprint parametrizations (still with a parallel beam) has been already tested in an earlier stage of the

analysis, showing an effect not exceeding 30% [21]. The actual beam footprint hitting the MEGAPIE target will be known when a detailed gamma-spectrometry mapping is performed on the irradiated MEGAPIE window. However, this gamma mapping will only give the integrated beam footprint over four months of operation, not the instantaneous beam profile.

4.1.2. Influence of the spallation models

Spallation reactions are modeled by a two or three step process. The first step is the direct interaction of the incoming proton with the target nucleus, described by an intra-nuclear cascade model, leading to the emission of high energy particles and to an excited remnant nucleus. Then, the de-excitation of the nucleus is described by a fission-evaporation model. In some cases, an intermediate step, called pre-equilibrium, can be added in the simulation to better take into account the energy balance before the de-excitation of the remnant nucleus. These steps are often treated by different models in simulation codes. The impact of using different spallation treatments in MCNPX has been studied by comparing the results obtained with different intra-nuclear cascade models (Bertini[27], ISABEL[28] and INCL4[29]), coupled with the different de-excitation models (Dressner or ABLA[30]), as well as with the CEM2k[31] cascade/de-excitation model.

The results of these different simulations are given in table 11 (for the flux) and 12 (for the reaction rates) where one can note that the sensitivity of the spallation models on the neutron flux is lower than 10% for all of the detector positions. Neutron flux estimations given by the INCL4-ABLA model are systematically 5% to 8% lower than the values predicted by the MCNPX default Bertini-Dressner treatment, while the other two models (ISABEL-ABLA and CEM2k) systematically give values which are 2% to 5% greater than the reference. These results are in agreement with a previous study made using a simplified MEGAPIE geometry [21]. The overall shape of the neutron spectrum is not very sensitive to the different models, as can be seen from the fact that, for a given reaction, almost all effective cross-sections (table 12) vary only within the statistical fluctuations from one model to another. In the case of the two reactions on the Ni foil however, the dispersion observed is greater, 13% around the average value given by the four spallation treatments.

Table 11: Simulated neutron flux per mA at the 5 different positions inside the neutron detector ($\widetilde{\phi}$ is in n/cm^2/s/mA) for different spallation models (labels are BD for Bertini/Dressner, INCL for INCL4/ABLA, ISA for ISABEL/ABLA, and CEM for CEM2k).

Position	1 (Gd)	Monit.	2	4
$\widetilde{\phi}_{BD}$	5.68 10^{13} (0.5%)	4.25 10^{13} (0.9%)	3.36 10^{13} (0.7%)	8.47 10^{12} (1.0%)
$\Delta(\widetilde{\phi}_{INCL})/\widetilde{\phi}_{BD}$	-6%	-8%	-5%	-6%
$\Delta(\widetilde{\phi}_{ISA})/\widetilde{\phi}_{BD}$	+ 2%	+ 3%	+3%	+4%
$\Delta(\widetilde{\phi}_{CEM})/\widetilde{\phi}_{BD}$	+3%	+5%	+3%	+3%

Table 12: Simulated effective cross-sections (in barns) at different positions inside the neutron detector for different spallation models (labels are BD for Bertini/Dressner, INCL for INCL4/ABLA, ISA for ISABEL/ABLA, and CEM for CEM2k).

Position	Reaction	$\overline{\sigma}_{BD}$	$\overline{\sigma}_{INCL}$	$\overline{\sigma}_{ISA}$	$\overline{\sigma}_{CEM}$
AlCo foil	^{59}Co(n,γ)^{60}Co	1.09 10^{1} (5%)	1.07 10^{1} (5%)	1.06 10^{1} (5%)	1.08 10^{1} (5%)
Fe foil	^{58}Fe(n,γ)^{59}Fe	2.9 10^{-1} (6%)	3.0 10^{-1} (6%)	2.9 10^{-1} (6%)	2.7 10^{-1} (6%)
Ni foil	^{58}Ni(n,p)^{58}Co	1.6 10^{-2} (6%)	1.6 10^{-2} (6%)	1.8 10^{-2} (6%)	1.4 10^{-2} (6%)
	^{60}Ni(n,p)^{60}Co	2.2 10^{-3} (7%)	2.1 10^{-3} (7%)	2.3 10^{-3} (7%)	1.9 10^{-3} (7%)
Pos. 1	^{235}U(n,f)	1.01 10^{1} (2.5%)	1.04 10^{1} (2.5%)	1.00 10^{1} (2.5%)	1.02 10^{1} (2.5%)
Pos. 2	^{235}U(n,f)	2.04 10^{2} (2%)	2.06 10^{2} (2%)	2.02 10^{2} (2%)	2.07 10^{2} (2%)
Pos. 4	^{235}U(n,f)	3.02 10^{2} (3%)	3.02 10^{2} (3%)	3.04 10^{2} (3%)	3.10 10^{2} (3%)

4.2. Epithermal neutrons

Epithermal neutrons are mostly generated by neutron scattering in the LBE and on structural materials, or by high energy spallation neutrons which have not been fully thermalized in the moderator. Thus, the epithermal measurement provided by the FC (Gd shielded) in position 1 yields information on both neutron production and neutron transport within the target. Therefore, the already mentioned discrepancy of about a factor 2 between the simulated and the experimental results is compatible with the considerations made previously for fast neutrons, showing that this discrepancy comes mainly from neutron production.

4.3. Thermal neutrons

Neutrons are thermalized within the D_2O moderator, essentially by multiple scattering on deuterium nuclei, and finally get the energy corresponding

to the thermal motion of the D_2O molecules, given by the absolute temperature of the moderator (305 K - 310 K). In order to be detected, thermal neutrons have to pass back through at least 5 cm of hot LBE (in the range 510 K - 650 K) and a number of structural materials before reaching the neutron detector (which is almost at the same temperature than the LBE). Therefore, the thermal neutron flux measured by the fission chambers does not depend only on the neutron production but is also sensitive to the transport conditions. In order to quantify this sensitivity, the influence of the temperature and of the geometrical description of the target have been studied.

4.3.1. Influence of the temperature

The temperature acts on the neutron reaction cross sections in two ways: the Doppler broadening of the cross-section resonances and the displacement of the thermal equilibrium peak in the neutron energy distribution.

The Doppler broadening comes from the thermal motion of the target nucleus which is added to the relative motion of the nucleus with respect to the interacting neutron. It affects resonances and plays a significant role when considering macroscopic effects of neutron transport inside a thick material, such as the self-shielding of average cross-sections inside fuel rods, but however, conserves the integral value of the cross-section. In our case, FC deposits are only a few nm thin layers of ^{235}U oxide and the Doppler effect on the average ^{235}U absorption cross-section is expected to be negligible. This has been verified by comparing the results of the simulation using the data libraries processed at 300 K and 800 K for ^{235}U reaction cross sections. No difference outside the statistical error of the simulation has been observed in the average cross-sections.

All simulations have been performed using a temperature of the D_2O moderator of 300 K, instead of 310 K (maximum value), for the Fermi gaz treatment. This induces a little shift in the Maxwellian peak toward lower energies, increasing the calculated average reaction cross sections. We estimated the bias introduced by this assumption to be less than 2%. Moreover, changing in the simulation the temperature of the LBE from 300 K to 700 K has shown no impact on the calculated average cross-sections. This can be understood considering that the neutron interaction lenght in the LBE is much higher than the thickness of the crossed LBE.

A third phenomenon related to temperature and which is, in our case, the most significant effect, has been already mentioned in section 2.3 and

concerns the thermal expansion of the structural materials. In the case of the neutron detector in operating conditions, this effect has been quantified to be a vertical shift of around 1.4 cm [22]. As an order of magnitude, an upward vertical shift of 1 cm in the position of the detector results in a decrease of around 3% on the value of the total neutron flux while keeping the shape of the spectrum unaffected.

4.3.2. Influence of the geometrical description

In order to establish how much the simulated neutron flux inside the LBE is sensitive to a detailed description of the MEGAPIE environment, we have compared the results given by the reference model with two other geometrical models of MEGAPIE (named S1 and S2 in figure 16) which present major modifications :

- The S1 model [32] includes the moderator tank geometry where all the neutron beam lines are removed. The target head is replaced by a block of steel. The description of the rest of the target, including the inner neutron detector, is unchanged from the reference.

- The S2 model[1] provides a very detailed description of the moderator tank including all the beam lines but all structures or shielding outside of the moderator tank are removed. There is no description of the central rod within the target, whose volume is entirely filled with LBE. In this geometrical arrangement, since the target is cut at the tank level, the LBE volume is smaller than in the real case; however, the "active" LBE volume, where primary neutron production occurs, is in any case unchanged from the reference.

In all cases, the same reference LBE composition and proton source description have been used. The simulated neutron flux spectra at the 2nd position in the neutron detector are presented in figure 17 for the two simplified models, compared to the reference. The S1 model shows a more thermalized spectrum: around 20% more than in the reference case. This is mostly due to the absence of beam lines because neutrons that would normally escape through these lines are indeed thermalized in the tank. On the other hand, the S2 model overestimates neutron leakages by not taking into account the

[1]The S2 geometry is taken from the model developed by E.Pitcher from LANL.

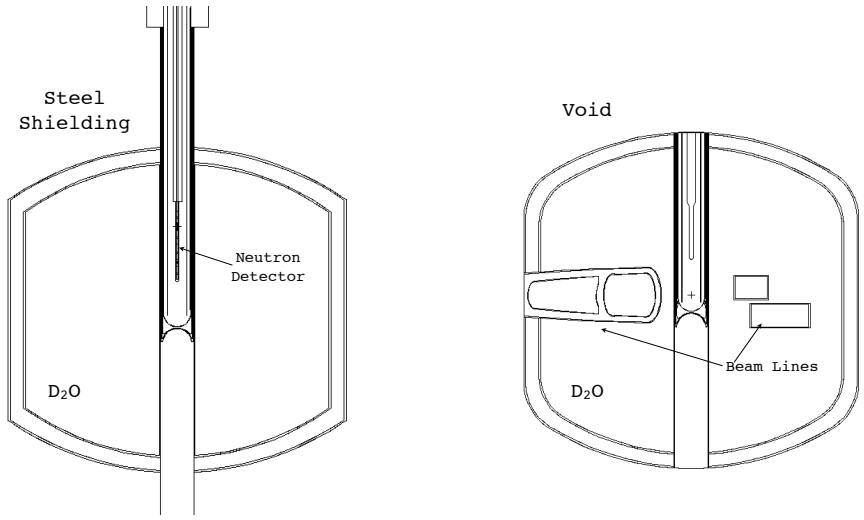

Figure 16: S1 (left) and S2 (right) simplified geometrical models of the MEGAPIE target shown in a vertical cut. S1 is surrounded by steel shielding whereas S2 does not consider any propagation of neutrons outside of the tank's volume.

back-scattering on the shielding around the tank and on the upper part of the target itself. In the S2 model, neutrons exiting the moderator tank are lost, and we see an overall decrease of the neutron population (from 20 to 30%) over the whole energy range.

It is interesting to note that, if we plot the evolution of $\widetilde{\phi}$ along the target's vertical axis (figure 17), the neutron flux calculated in the reference case lies between the two simplified cases. Although the S1 and S2 models are clearly only rough approximations of the real case, the calculated neutron flux inside the central rod does not differ by more than 30% to the reference value and still overestimates the measured values of $\widetilde{\phi}$. This is shown in figure 18 where the measured and the simulated values of the neutron flux are given as a function of their vertical position.

Since these major simplifications of the geometry have a limited impact (in comparison to the observed C/E discrepancies) on the neutron production capabilities of the target, it is rather unlikely that the origin of the C/E

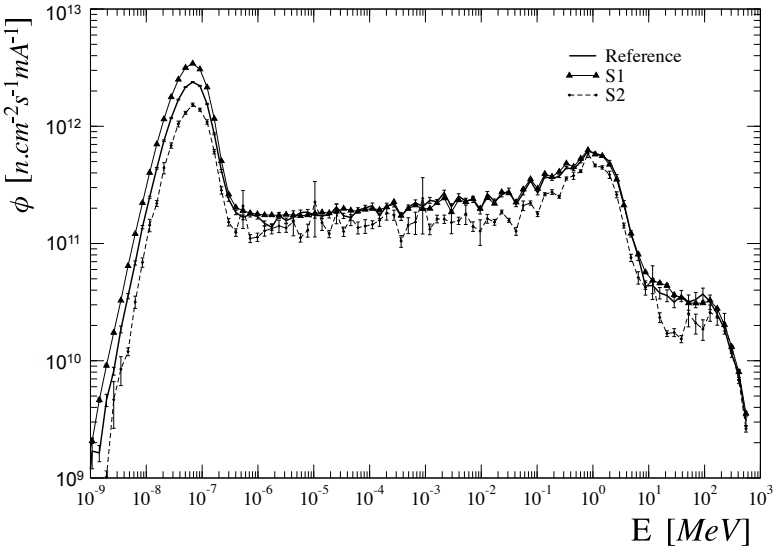

Figure 17: Neutron spectrum at position 2 for the 3 different models. The S2 model does not take into account any back-scattering of neutrons escaping the moderator tank volume : epithermal and fast neutron population is poorly described, as shown by the larger statistical fluctuations.

discrepancies comes from an erroneous or poor description of the structural geometry. On the contrary, the study of these different models shows that a simplified geometrical description of the target can have a non negligible influence on the neutronic performances and that the most accurate description is needed when modeling such a complex system.

4.3.3. Impact on ADS design

The most interesting and unexpected conclusion that we can work out from this study is that the neutron fluency at a given position, close to the region where spallation neutrons are produced, is not only sensitive to the spatial profile of the beam, but also to its angular distribution. Because of the absence of a spatial monitoring of the beam, the actual angular distribution of incoming protons which irradiated the MEGAPIE target is unknown and the actual beam footprint of MEGAPIE will only be obtained when a detailed gamma-spectrometry mapping is performed on the irradiated window.

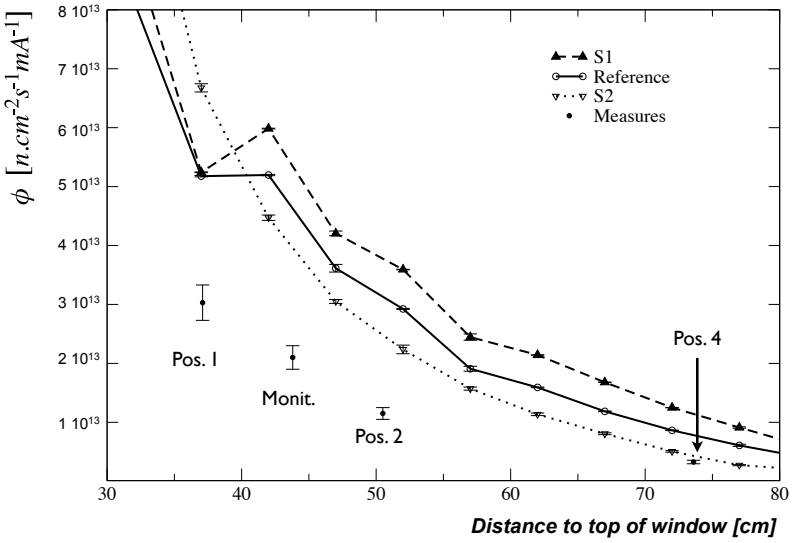

Figure 18: Evolution of $\widetilde{\phi}(z)$ along the target's vertical axis for the 3 geometrical models, S1, S2 and the reference. The depression around $z = 35$ cm, which is due to the Gd shielding, is observed in the reference and S1 models, which implement the neutron detector description inside the central rod.

For an unmoderated system such as an ADS, the neutron flux at a given position inside the target is expected to be even more sensitive to the angular description of the incoming proton beam. In the absence of moderation, high-energy neutrons inside the target will come mainly from the spallation region, and their direction will be strongly related to the axis of the primary proton-nucleus interaction. As a simple illustration, figure 19 shows the simulated vertical profile of the neutron flux in the case of a flat ($\theta = 0$) or a divergent ($\theta = 800$ mrad) proton beam for a unmoderated LBE target. One can notice a valuable modification of the neutron production peak, while the spatial development of the cascade is kept within the target. In this simple example, a neutron detector placed at a given position along the target axis can be very sensitive to the neutron flux variation due to the beam spread. Another safety aspect related to the proton beam focus control concerns a possible unwanted interaction of the high energetic protons directly within

the fuel element, which may lead to a modification of the composition of the fuel or its shielding and affect the decommissioning of the system.

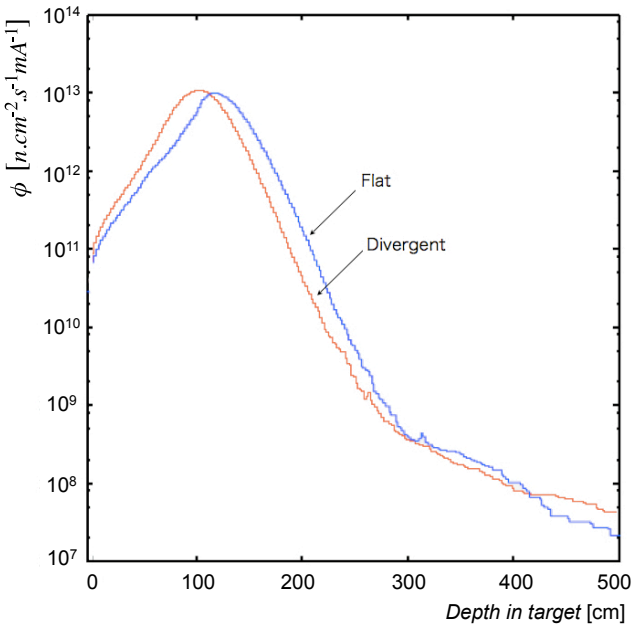

Figure 19: Simulation of the neutron flux profile for an unmoderated target irradiated by a flat and a divergent beam.

5. Conclusions

The MEGAPIE target was successfully irradiated for four months in 2006, demonstrating the reliability of a high power liquid metal target and providing fundamental data for future targets and ADS design. An innovative neutron detector based on micrometric fission chambers was built and operated successfully during the whole MEGAPIE irradiation, providing reliable measurements of the neutron production inside the target and its variation in time all along its operation. Coupled with the analysis of activation foils, the results extracted from the neutron detector data allowed a thorough study of the neutronic performances of the target versus the proton beam. A significant discrepancy between measurements and simulation has been found and triggered a deep sensitivity study of the key parameters of the simulation.

It has been shown that several factors play an important role in the neutron generation and in the neutron transport; in particular, a detailed description of the system geometry and the related materials is essential to provide reliable estimation of the different energy contributions to the neutron flux and to correctly estimate backscattered neutrons and neutron leakages in the complex structure of MEGAPIE. Different spallation models were also compared and showed to give consistent results within 10% in all cases. However, these factors are not able to fully explain the observed discrepancies. The most influent parameter, likely to be the main source of discrepancy, is the proton beam description. In particular, the reference simulated proton beam did not take into account an angular distribution of the incoming protons at the window level. From the MEGAPIE neutronic experience, it clearly appears that the simple monitoring of the beam intensity is not sufficient in such a complex system. As a recommendation for future spallation target design and development, it is important to stress that the monitoring should also include a detailed beam profiling. A precise monitoring of the neutron production can therefore be achieved in order to keep the target on its best performance. This is even more important when the target is used as an external source for a sub-critical reactor since an undetected change on the beam focusing may lead to local unexpected increase of the neutron production which directly affects the safety of the system.

6. Acknowledgments

This work has been performed in the context of the EU-programs FIS5-2001-00090 with the acronym MEGAPIE-TEST. Part of the equipment has also been supported by the French GEDEPEON funding. The authors are grateful to the PSI team for their efficiency during operation and dismounting of the neutron detector.

References

[1] http://www.eurisol.org and references therein

[2] R.L. Burman and W.C. Louis, *Jour. Phys.* G 29 (2003) 2499–2512

[3] E. H. Lehmann, *Neutron Imaging Methods and Applications*, Springer Science (2009)

[4] M. Salvatores, *Jour. Phys. IV* France 09 (1999)

[5] G.S. Bauer et al., *Jour. of Nucl. Mat.* 296 (2001) 17-33

[6] G.S. Bauer et al., *Jour. Phys. IV* France 12 (2002)

[7] D. Hilscher et al., *Nucl. Instrum. and Meth.* A414 (1998) 100-116

[8] A. Letourneau et al., *Nucl. Instrum. and Meth.* B170 (2000) 299-322

[9] S. Leray et al., *Phys. Rev.* C65 (2002) 044621

[10] J.P. Meulders, A. Koning and S. Leray, HINDAS final report EU FIKW-CT-2000-00031 (2005)

[11] L. Zanini et al., *Neutronic and Nuclear Post-Test Analysis of MEGAPIE,* PSI Bericht Nr.08-04 2008

[12] S. Panebianco et al., *Ann. Nucl. Energy* 36 (2009)

[13] D. Reggiani, Private communication

[14] Pelowitz et al., *MCNPX user's manual - version 2.5.0.* LANL (2005)

[15] C. Fazio et al., *Nucl. Eng. and Des.* 238 (2008) 1471-1495

[16] S. Chabod et al., *Nucl. Instrum. and Meth.* A566 (2006) 633-653

[17] A. Letourneau et al., Proceedings of the International Conference ANIMMA (Marseille, France), IEEE 2009, in press

[18] O. Bringer, PhD Thesis, Institut National Polytechnique de Grenoble, October 2006

[19] S. Chabod, PhD Thesis, Université de Paris XI, Orsay, November 2006

[20] S. Chabod et al., *Nucl. Instrum. and Meth.* A562 (2006) 618-620

[21] S. Panebianco et al., Proceedings of Internation Conference ACCAPP-07 (Pocatello, USA), 2007

[22] A. Cadiou, *Thermal Expansion of The Target*, Technical Note Q-MEG-2.01-M-DI-010-F (2003)

[23] A.J. Koning et al., Proceedings of International Conference ND2004 (Santa Fe, USA), AIP 769, 2005

[24] M. Dierckx, *MEGAPIE Thermohydraulic Post Test Analysis*, SCK-CEN-R-4537 (2007)

[25] W.B. Wilson et al., *A Manual for CINDER90 Version 07.4 Codes and Data*, Technical Report LA-UR-07-8412, LANL (2007)

[26] U. Rohrer, *p-Strahlbreiten unp Profil-Formen beim SINQ-Target mit und ohne Target E*, PSI internal report (2001)

[27] H.W. Bertini, *Phys. Rev.* 188 (1969) 1711

[28] K. Chen et al., *Phys. Rev.* 166 (1968) 949

[29] A. Boudard et al., *Phys. Rev.* C66 (2002) 44615

[30] A. R. Junghans et al., *Nucl. Phys.* A629 (1998) 635

[31] S.G. Mashnik et al., *Nucl. Instr. and Meth.* A414 (1998) 68

[32] F. Michel-Sendis et al., Proceedings of International Conference ICRS11 (Pine Mountain, USA), 2008, in press